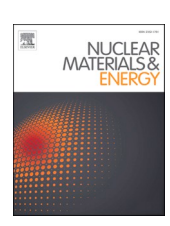
ELSEVIER

Contents lists available at ScienceDirect

Nuclear Materials and Energy

journal homepage: www.elsevier.com/locate/nme



Deuterium retention in sputter-deposited W-B layers: in-situ implantation and ion beam analysis during annealing[★]

D.N. Gautam ^{a,*} , T.T. Tran ^a, M. Fellinger ^b, F. Aumayr ^b, M. Rubel ^{a,c}, D. Primetzhofer ^a, E. Pitthan ^a

ABSTRACT

Boronization in tokamak devices with tungsten (W) plasma facing components (PFC) may lead to the formation of mixed layers of W and boron (B) that can affect wall retention of plasma fuel species. In this study, deuterium (D) retention was investigated in W-B thin films with different stoichiometries as well as in pure W and B, grown on silicon (Si) substrates by means of magnetron sputter deposition. After pre-characterization, the layers were implanted with 1 keV D_2^{\pm} ions to a fluence of 7×10^{17} D/cm², followed by in-situ ion beam analysis. The samples were annealed to temperatures between 400–600 °C and in-situ ion beam analysis measurements were performed before, during and after the annealing process by simultaneous Elastic Recoil Detection Analysis and Rutherford Backscattering Spectrometry. The different B concentrations in the films led to significant differences in D retention, where higher boron concentrations resulted in higher deuterium retention immediately after implantation. After annealing, the lowest amount of retained D was observed for a W-to-B ratio of 2:1, with an areal density of 8×10^{13} D/cm², about three times lower than for pure W. The highest retention of around 5×10^{16} D/cm² after annealing to 600 °C was found for the pure B-film. Ex-situ electron microscopy techniques revealed significant morphological modifications due to implantation and/or annealing, including bubble formation (W film), W surface enrichment (B-rich film) and crack formation (W-rich film).

1. Introduction

PFC in tokamak devices such as ITER are exposed to extreme radiation and heat loads during operation [1–3]. The foreseen fuels used for the fusion reactions in future tokamak devices are deuterium (D) and tritium (T) that combine to form alpha particles and high energy neutrons, the latter of which will be used for energy production in future fusion power plants. Due to the scarcity and radioactivity of T it is crucial to choose a plasma facing material (PFM) with low retention of light elements since high levels of fuel retention could negatively impact reactor performance, lifetime and safety [4]. Tungsten (W) fulfills this and additional requirements of a PFM, having for example a high melting point and low sputter yield. It was recently announced that W is replacing beryllium (Be) as PFM in ITER in the new baseline [5,6] and is already in use in other devices [7,8].

The presence of mid-Z impurities like oxygen can be expected in any fusion device [9,10]. These impurities will degrade the plasma and may act as a seed for sputtering W and other high-Z elements, leading to significant radiation losses in the core plasma and can in the worst-case

lead to disruptions [11,12]. W does not provide the same level of oxygen gettering properties such as those of Be, therefore, alternative methods of impurity reduction must be used. A glow discharge conditioning (GDC) technique, commonly referred to as boronization, will be used for ITER [13]. The technique was developed for TEXTOR [14] and has been successfully implemented in several fusion reactors since then [15–17]. In tests done at the WEST tokamak it was observed that boronization significantly improved plasma stability and was in some cases even necessary for plasma startup [8]. During boronization, a thin film containing boron (B) is deposited on the entire first wall (FW) and divertor regions in order to getter impurities. The deposition can be done in different ways, such as solid boron injection [18] or boronization via pulsed ion cyclotron wall conditioning plasma [19,20]. Proposed for ITER is a glow discharge with (deuterated) diborane (B_2D_6) [6].

An unwanted side-effect of the boronization may be the formation of tungsten-boron (W-B) mixtures through continuous re-deposition steps during plasma wall interactions (PWIs). The presence of W-B mixtures has already been observed on ITER-like PFC in WEST [21]. The formed W-Bs feature different stoichiometries, morphologies and

E-mail address: daniel.gautam@physics.uu.se (D.N. Gautam).

^a Department of Physics and Astronomy, Ångström Laboratory, Uppsala University, Box 516, SE-751 20 Uppsala, Sweden

b Institute of Applied Physics, TU Wien, Fusion@ÖAW, 1040 Vienna, Austria

^c Department of Fusion Plasma Physics, KTH Royal Institute of Technology, 10044 Stockholm, Sweden

 $^{^{\}star}$ This article is part of a special issue entitled: 'PFMC-20' published in Nuclear Materials and Energy.

^{*} Corresponding author.

Table 1

Description of samples. The B-concentrations of the films were estimated with ToF-ERDA measuements. The sputter yields were calculated by SRIM and SDTrimSP and film densities and backscatter rates calculated by SRIM. Film thicknesses are measured with TEM or estimated based on the listed film densities (SRIM) together with ToF-ERDA data. The implantation fluences are approximated using the average current measured by the sample holder during implantation.

Sample name	W	W ₂ :B	W:B	W:B ₉	В
B concentration (at. %), ToF-ERDA	0	~37	~50	~90	96
Film thickness (nm), TEM	181	235	126	150*	149
Film density (g/cm ³), Experimental	18.7	17.0	16.2	_	2.47
Film density (g/cm ³), SRIM	19.35	14.93	10.00	4.05	2.35
Impl. Fluence (10 ¹⁷ D/ cm ²)	6.16	7.42	6.19	7.27	7.00
Sputtered B (at./ion), SRIM	_	0.085	0.0186	0.0338	0.035
Sputtered B (at./ion), SDTrimSP	_	0.030	0.036	0.036	0.022
Sputtered W (at./ion), SRIM	0	0.00180	0.00243	0.00051	-
Sputtered W (at./ion), SDTrimSP	0.002	0.001	0.001	6E-5	-
Backscatter yield (%), SRIM	44	38	34	15	6.5

^{*}Thickness estimated by ToF-ERDA and RBS together with the film density approximations calculated by SRIM.

microstructures that can behave differently from the pure elements during device operation. Boron is also known to have strong retention properties of hydrogen isotopes [22,23], that may affect the retention properties of the formed W-Bs.

There exist a few different methods to remove hydrogen isotopes retained in PFC [24]. One such method is called strike-point scanning and has been shown to reduce the D content of thick co-deposits in the divertor region of JET [25]. Baking is another method for recovering D and T as well as removing impurities that are retained in the walls of a reactor. Baking has been utilized as a wall conditioning method by several tokamaks [24,26,27] and is expected to be used in ITER as well [12]. For ITER, no plans exist for infrastructure that would allow baking of PFC to temperatures above 240 °C [12]. Surface temperatures of PFC are however expected to reach temperatures of 600 °C [28] or even above 900 °C [29] in some parts of the reactor during nominal operation. To investigate the potential impact of the mixing of B and W and its effects on hydrogen isotope retention and desorption during annealing, W-B thin-films of different stoichiometries were grown followed by insitu D implantation of the films. To avoid D loss from air exposure, insitu Ion Beam Analysis (IBA) was used to monitor, in real time, the D retention in films before, during and after annealing. Further characterization was done ex-situ using electron microscopy imaging techniques to study the changes in morphology of the films after implantation and annealing.

2. Materials and methods

This experimental study was performed at the Ångström Laboratory at Uppsala University using the facilities of the Tandem Laboratory to produce, anneal and analyze films using IBA techniques and the facilities of the Myfab laboratory for microscopy imaging of the films.

2.1. Growth of W-B layers

A PREVAC magnetron sputtering system was used to grow W-B thin films of different stoichiometries [30]. The magnetron system was recently upgraded and is now equipped with four MS2 63C1 magnetron

sources suitable for targets with 2" diameter and 1-6 mm thickness. Five different depositions were performed to obtain W-B films with different stoichiometries. The general procedure was the same for all depositions and is described in the following. The substrates used were silicon (Si) < 100 > wafers, 1 cm² in size, which were all ultrasonically cleaned for 10 min in an ethanol bath prior to transfer into the sputtering system. Starting from a base pressure between 5 \times 10 $^{\text{-8}}$ and 4 \times 10 $^{\text{-7}}$ mbar, Argon (Ar) was introduced into the chamber to act as sputtering gas during the depositions. All depositions were performed at room temperature at a pressure of 5.6 \times 10⁻³ mbar. Sputter co-deposition using two magnetron targets simultaneously was used to grow the mixed W-B films. The power supplied to the magnetrons depended on the desired film composition and varied between 0-170 W for the boron target and 0-50 W for the tungsten target, both operating with radiofrequency (RF) discharges. A quartz crystal microbalance (QCM) was used to measure the deposition rate and estimate the final thicknesses of the films. The samples were named according to the W-to-B ratio determined experimentally of the films, as presented in Section 3, Table 1.

2.2. Characterization of W-B layers and implantation of D

With the films deposited, the samples were removed from the sputtering system and transferred to beamline T6 of the MV NEC-5SDH-2 pelletron tandem accelerator of the Tandem Laboratory (described in [31]), where the film compositions and purities of the as-deposited films were determined with time-of-flight elastic recoil detection analysis (ToF-ERDA). D implantation and in-situ IBA during annealing of the samples was subsequently conducted in the Set-up for In-situ Growth, Material modification and Analysis (SIGMA) [32] chamber which is one of the end stations of the pelletron tandem accelerator at the Tandem Laboratory. The setup enables e⁻-beam, low-energy ion implantation of samples in an ultra-high vacuum (UHV) environment using a plasma ion gun heating as well as simultaneous IBA. Base pressure during all measurements was around 5 \times 10⁻⁸ mbar and during the implantations around 6×10^{-6} mbar due to the introduction of D-gas into the chamber. A residual gas analyzer (RGA) used to monitor the atomic mass distribution of the species in the chamber throughout all measurements confirmed mainly the presence of deuterium during implantation. The ion gun was used to implant the samples with predominantly 1 keV D₂⁺, corresponding to 500 eV/D, assuming first that the majority (93 %) of the implanted species is molecular (D₂⁺) [33,34] and second that the incident D_2^+ molecules are all dissociated before reaching the sample surfaces [35]. The implantations were done at normal incidence to the sample surfaces. A nominal fluence of 7×10^{17} D/cm² was targeted in all implantations. For the post-characterization of the films using scanning electron microscopy (SEM), part of the surface of the samples were intentionally covered during the implantation procedures. The covered parts of the films were thus not implanted with D, but were annealed to the same temperatures as the implanted regions, allowing for comparison of the two regions to investigate the effect of D-implantation on the morphologies of the films.

2.3. In-situ ion beam analysis during annealing of D-implanted W-B

Following implantation, annealing of the samples was conducted combined with in-situ IBA to measure the D retention in the films. Elastic recoil detection analysis (ERDA) and Rutherford backscattering spectrometry (RBS) measurements were performed using a primary beam of 2.13 MeV $^4\text{He}^+$ ions that was used to obtain depth profiles of the samples. The specific energy of the primary beam was selected to make use of the elastic resonance (~70 keV FWHM) for the nuclear reaction D(α , D) ^4He , that improves the detection sensitivity of D during analysis [36]. The ERDA provided information about the quantification and depth distribution of H and D in the samples while the RBS analysis yielded complementary information about the composition and thickness of the films. These IBA techniques were utilized to perform in-situ pre-

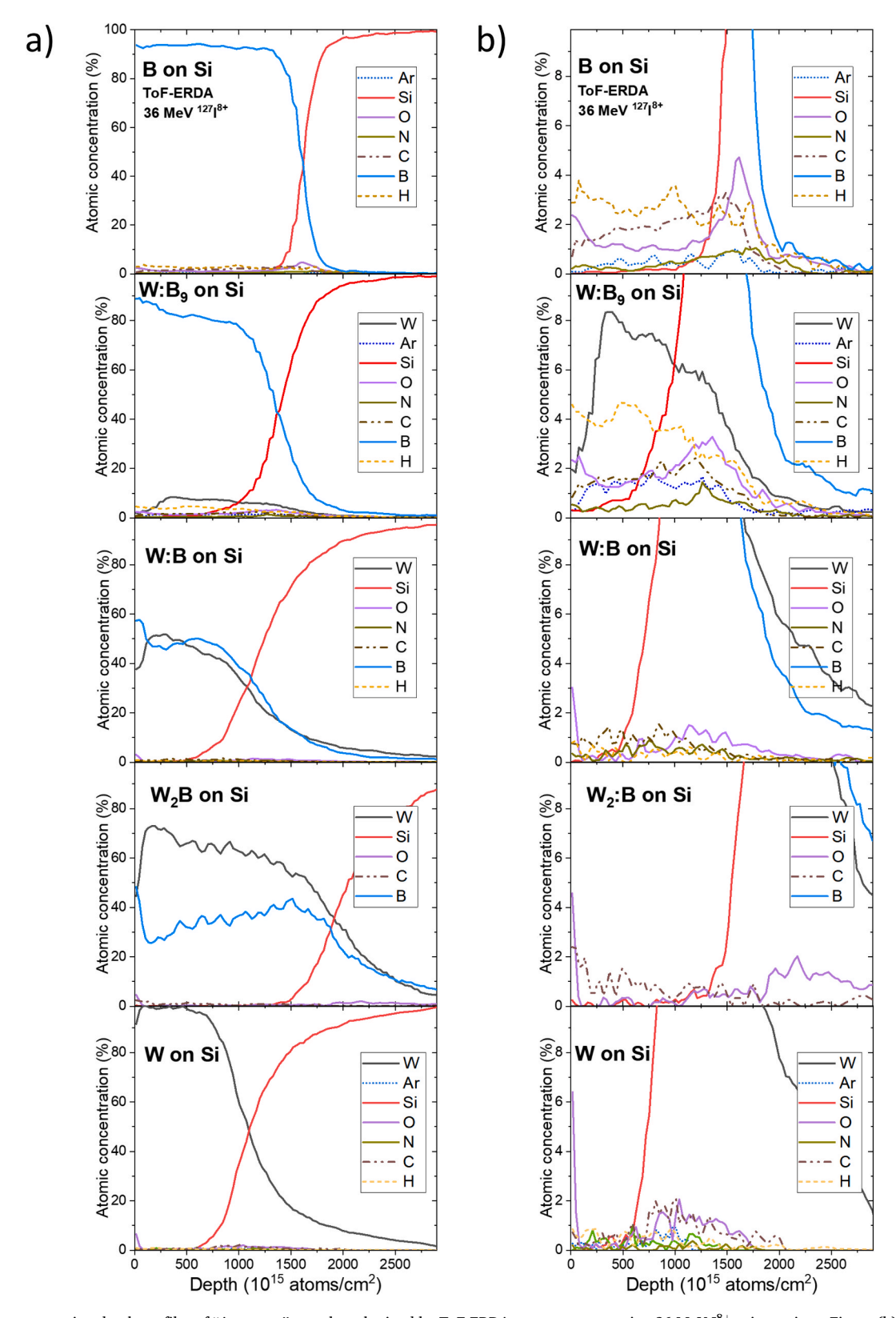


Fig. 1. Atomic concentration depth profiles of "As grown" samples, obtained by ToF-ERDA measurements using 36 MeV I⁸⁺ primary ions. Figure (b) shows presence of low concentration elements in more detail.

characterization of the samples directly following D implantation.

The samples were subsequently annealed while the D retention, distribution and composition of the films were simultaneously measured by ERDA and RBS. The detector geometry for the IBA measurements was set so that the primary beam was at an incidence angle of $\alpha=70^\circ$ with

respect to the surface normal, where both the ERDA and RBS detectors were placed at an exit angle $\beta=80^\circ$, again with respect to the sample surface normal, both in IBM geometry. The ERDA detector resided thus at a scattering angle of $\theta=30^\circ$ and the RBS detector at $\theta=170^\circ$, both with respect to the incident beam direction, see Appendix A Fig. 1 for a

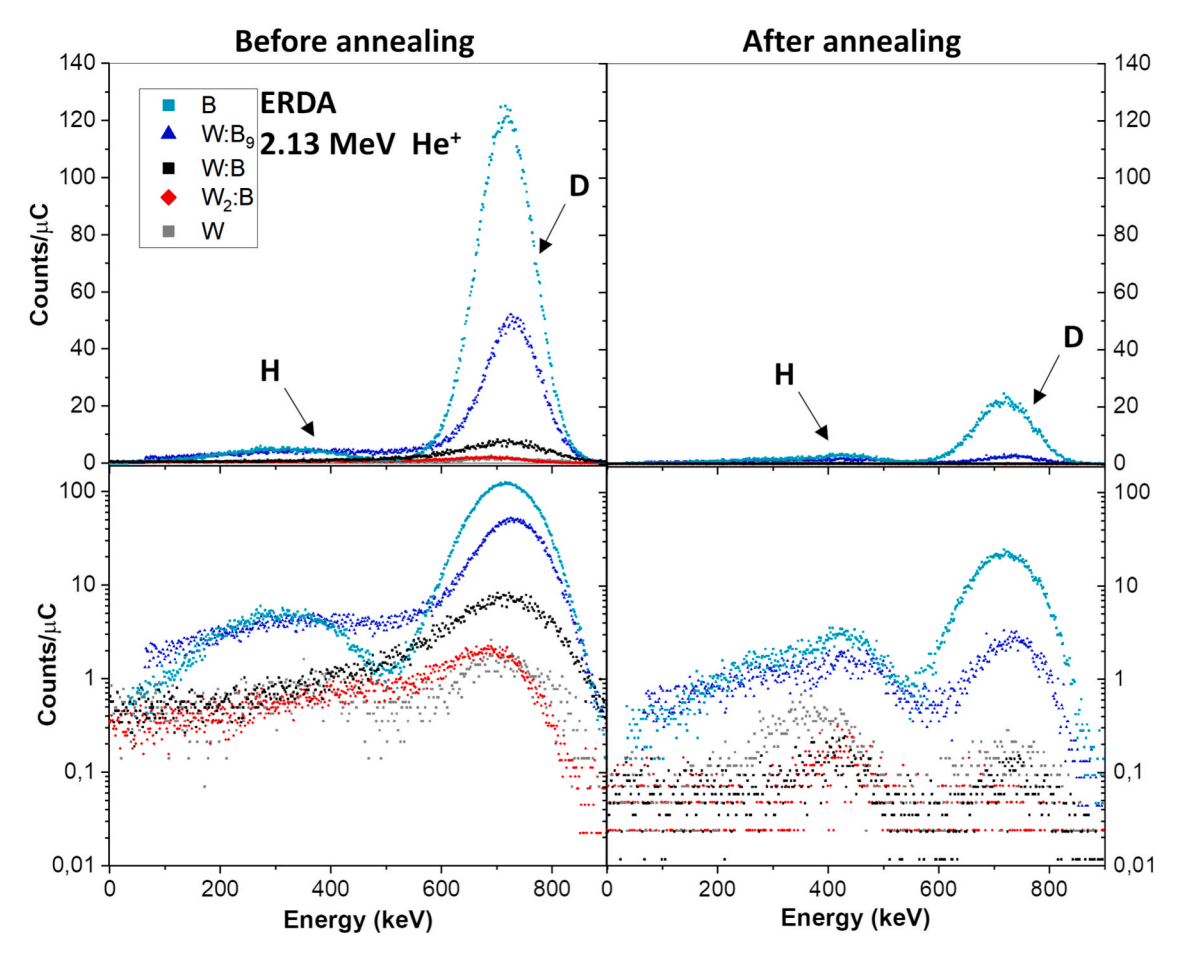


Fig. 2. Experimental ERDA-spectra showing the charge normalized yield of H and D before (left) and after (right) annealing of the samples. The same spectra are shown with a linear (top) and logarithmic (bottom) y-axis.

schematic illustration of the setup. Absorber foils were placed in front of the detectors to reduce unwanted signal/noise. The foil thickness in front of the ERDA detector was chosen to stop the scattered primary beam particles while still allowing for hydrogen and deuterium profiling. The absorber foil in front of the RBS detector reduced noise by blocking light from reaching the detector during sample annealing. The measurements started with the samples at room temperature (20 °C). The temperature was measured using two Optris CT 3 M pyrometers positioned outside the chamber and focused with lasers on the centers of the samples. The two pyrometers are rated for two different temperature ranges with some overlap (50–400 °C and 150–1000 °C). A temperature ramp close to 4.8 °C/min was kept for each annealing and was continued up to 600 °C or until the D signal was indistinguishable from read noise. A subsequent faster ramp down of the heating filament followed after reaching the temperature maximum and the sample was then allowed to cool down passively. The chamber pressure was around $\sim 10^{-7}$ mbar during the annealing procedures and $\sim 10^{-8}$ mbar before and afterwards.

In-situ post-characterization of the samples was also carried out after annealing once the sample was allowed to passively cool down to room temperature (below 50 $^{\circ}$ C). The residual D retention in the samples was quantified by simultaneous RBS and ERDA measurements using the same beam configuration and geometry as before/during annealing.

To analyze the collected data, the SIMNRA program [37] was used to provide simulated fits to the ERDA and RBS spectra from the experiments. The RBS analysis allowed for charge calibration which was used in order to obtain quantitative estimates of the H and D concentrations in the samples from the fits to ERDA profiles, using cross section data by Quillet et al. [36].

2.4. Ex-situ morphology analysis utilizing electron microscopy techniques

The morphology of the *Implanted & Annealed* films was investigated with a Zeiss Crossbeam 550 scanning electron microscope/focused ion beam (SEM/FIB) system and compared to twin samples from the same batch that were not implanted or annealed, from now on referred to as *As grown* samples. A focused beam of gallium ions was used to cut ultrathin lamellae of some of the films and scanning transmission electron microscopy (STEM) was used to image their cross-sections. This approach also allowed for determination of the film crystallinity (diffraction TEM), elemental homogeneity and thickness. Energy-dispersive X-ray Spectroscopy (EDX), using an Oxford Instruments AZtec EDS detector, supplemented the STEM imaging for elemental analysis.

To further investigate surface features seen with SEM for one of the samples, high-resolution RBS (HR-RBS) was measured using a semi-conductor surface barrier (SSB) detector with a cryogenic assembly installed at a scattering angle of 135° at a multipurpose beam line at the single stage 350 kV Danfysik implanter at the Tandem Laboratory, Uppsala University [38].

3. Results and discussion

3.1. Sample pre-characterization and simulation

Fig. 1 shows the depth profiles prior implantation for the 5 different samples used in this study. This pre-characterization confirms low contamination in the films and is used to estimate the W-B stoichiometries of the samples, listed in Table 1.

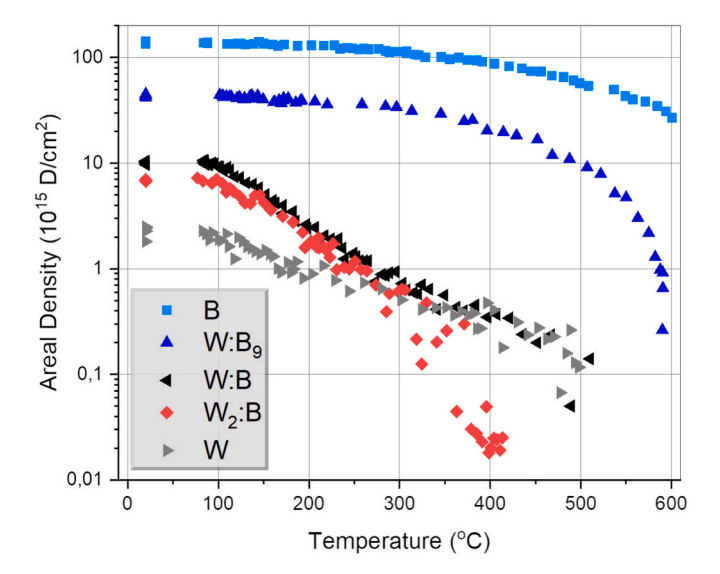


Fig. 3. Areal density of retained deuterium in the samples during annealing, as measured by ERDA. The areal densities were obtained by fitting simulated profiles to experimentally measured ERDA spectra using SIMNRA.

Implantation depth profiles were simulated for the different W-B stoichiometries, obtained from IBA, for 500 eV D irradiation using the binary collision approximation model SRIM [39]. In the simulated implantation depth profiles, the maximum ion range calculated for the different compositions, beyond which no ions should be expected according to SRIM, were all close to 2×10^{17} at./cm² (20–30 nm), with average ion ranges all around 0.5×10^{17} at./cm² (6–8 nm). The one exception was for pure B where the maximum range was around 4×10^{17} at./cm² (\sim 30 nm), with average ion range of 1.6×10¹⁷ at./cm² (11 nm). It is clear that all expected implantation ranges are well below the film thicknesses, shown in Table 1. However, the reader should be aware that SRIM has been demonstrated to potentially yield incorrect results such as overestimation of vacancy production [40] and unrealistic angular distribution of sputtered atoms [41], suggesting that the calculated ion ranges may not be accurate. This assumption is true in particular close to threshold energies as was used for the simulations in presented work, with 500 eV D⁺. Moreover, SRIM does not account for the mobility, saturation, diffusion or desorption of implanted species. Due to the high nominal implantation fluences, the depth profiles calculated by SRIM are unlikely to represent the final D profile in the samples.

Following sputter-deposition, the samples were temporarily exposed to atmosphere while being transferred to the UHV SIGMA chamber for in-situ implantation, IBA and annealing. In SIGMA, each sample was implanted with 1 keV D_2^+ ions using an ion gun, with nominal implantation fluences around 7×10^{17} at./cm². Each implantation lasted ~ 18 h with a beam current of around 5–6 μA , approximated using the average of current measured by the sample holder at the beginning and end of the implantations. By the end of each implantation the current had decreased by approximately 10 %.

Table 1 provides an overview of the samples, including their boron concentrations, film thicknesses, nominal total implantation fluences, the calculated sputtering yields for both tungsten and boron atoms, and the simulated fraction of deuterium ions that were backscattered during implantation. The backscattering (BS) yields, describing the reflection yield, or percentage of incident ions that are BS from the sample during the implantations, were calculated under the assumption that all incident particles during the experiments were charged D_2^+ ions and all backscattered species were neutrals. The BS yield is higher in W-rich films due to higher scattering cross-sections. The thicknesses of the films were estimated by IBA together with film density approximations calculated by SRIM. In the case of the B, W:B, W₂:B, and W films, the thicknesses were obtained by TEM, images can be found in Appendix A

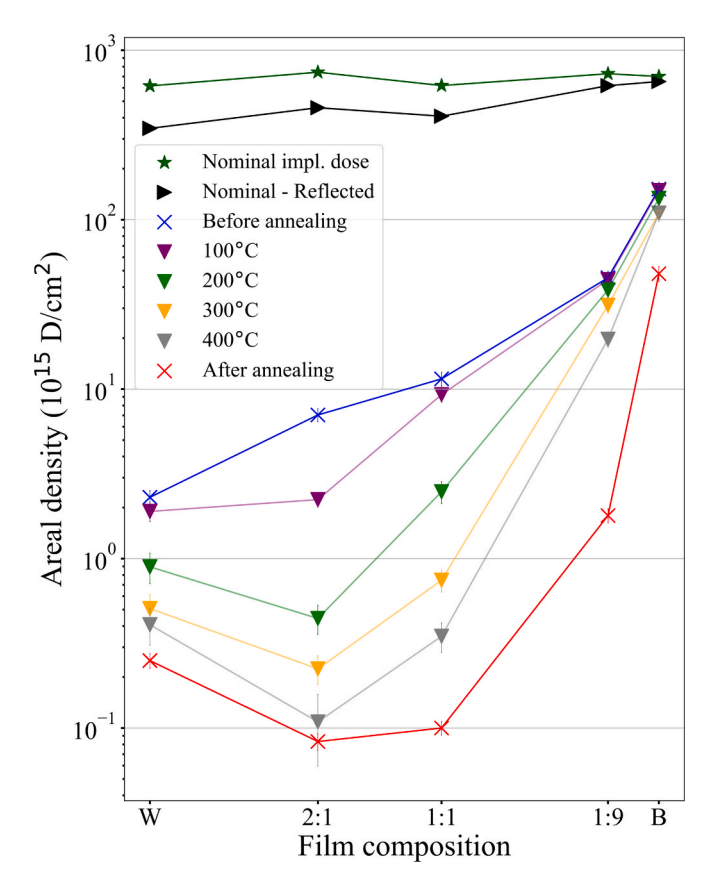


Fig. 4. Nominal implantation fluences and backscatter-corrected fluences, shown alongside the experimentally determined deuterium retention in each film before, during, and after annealing.

Figs. 2-5. Using TEM, the thickness of the W:B film was determined to be 126 nm, while using the ToF-ERDA measurement of the film together with density approximations from SRIM (as was done for the W:B $_9$ -film), a thickness of 191 nm is calculated instead. This discrepancy highlights the uncertainty in the thicknesses of the films for which TEM was not performed.

The W and B sputter-yields listed in the table were calculated by both SRIM and SDTrimSP [42]. The calculated sputter yields vary between the two different software packages, with SDTrimSP giving higher sputter yields in almost all cases. At low energy ion bombardment ($\sim 500~eV$) of W, SRIM is known to differ from experimental data, due to significantly higher default sputtering threshold energies used by the code, while much better agreement is observed in SDTrimSP [43]. According to SRIM calculations, no sputtering is expected in the case of pure W, which is unrealistic at this incident energy [41]. Nevertheless, such values can be used to estimate erosion of films due to the D implantation and compositional changes in the surface from preferential sputtering, as discussed later in this section.

3.2. Deuterium retention analysis

ERDA was performed to examine the concentration and distribution of H and implanted D in the films before, during and after annealing. Despite the fact that the implantation fluences were similar for all samples, the deuterium content was significantly different for each composition. The H which was also detected is assumed to be contamination present due to film exposure to air during transport between experimental set-ups. The ERDA spectra in Fig. 2 show the H and D profiles of the five samples before and after annealing. The peaks around 700 keV correspond to D retained in the samples while the peaks around 400 keV show retained H as well as, potentially, D retained deeper in the

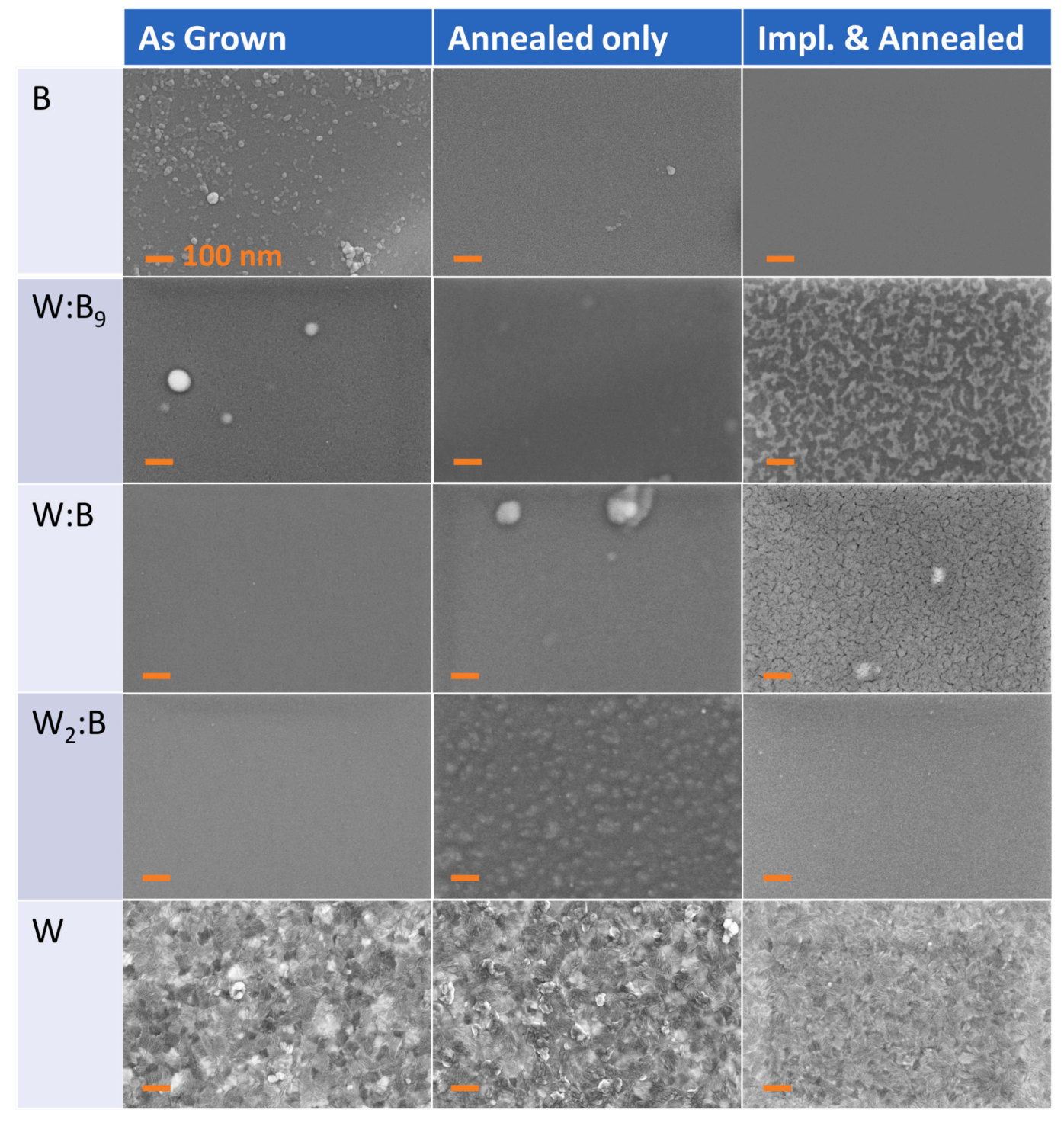


Fig. 5. SEM images of the film surfaces in three different states: "As grown" (neither implanted with deuterium nor annealed), "Annealed only" (annealed without D implantation), and "Implanted & Annealed" (subjected to both D implantation and subsequent annealing). All scale bars correspond to 100 nm.

films or substrates. The tails on the low-energy side of the D-peaks (the region around 500 keV, before overlap with H-signal), for the mixed films (W_2 :B, W:B and W:B₉) suggests that D has diffused deeper into the samples. From the spectra recorded after annealing, it is apparent that much or most of the implanted species were desorbed. Before annealing, directly after implantation, the amount of retained D in the samples is found higher in the B-rich films and scales with boron concentration. The same trend is not seen after annealing as both the W:B (black data points) and W_2 :B (red) films retained less D than the W film (gray).

Fig. 3 shows the D content in the films before and during annealing.

The collected data was split into sets of 100 s measurement time each, allowing for quantitative monitoring of the changes in H and D content at different temperatures. The data points at 20 °C show the D amounts in the films at the beginning of annealing before the samples reached a temperature measurable by the pyrometers (\sim 80 °C). The samples exhibit different retention behaviors at different temperatures. The Wrich films, W:B, W₂:B and W, lose D steadily starting around 100 °C and drop below detector read noise level around 400 °C (W:B) or 500 °C (W₂: B and W) at which point the samples were not heat treated further. The D retention is more stable in the B-rich films which were annealed up to

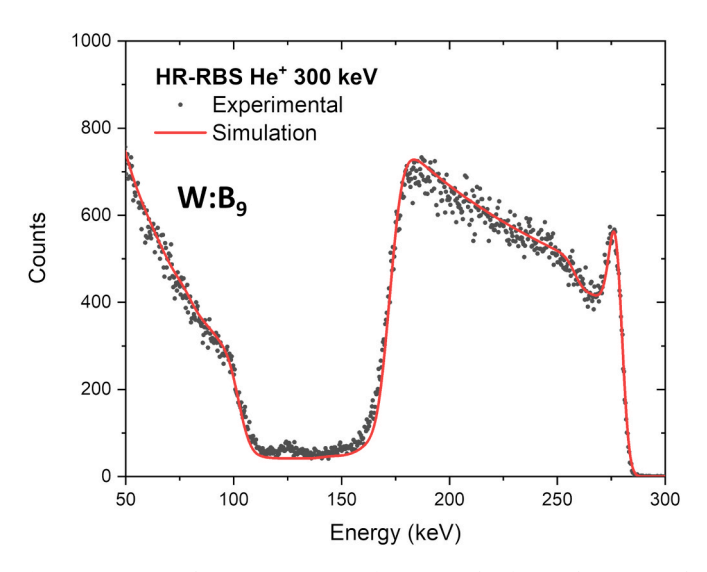


Fig. 6. Experimental HR-RBS spectrum of W:B₉ sample after implantation and annealing showing W-enrichment on sample surface. A simulated fit to data is also shown.

600 °C with a clear D signal still present in the ERDA spectra of both films at the end of the procedure. The D-distribution, seen in the ERDA measurements from before annealing, shows the presence of D deep in the film bulks/substrates of the samples with mixed films.

The retained amounts for all samples from before, after and during annealing for a few temperatures can be seen in Fig. 4. The 'nominal' and 'Nominal — Reflected' implantation fluence values are shown as well, where the latter refers to nominal yield minus the BS yield. The clear effect of B incorporation in the films can be observed. The retention behavior before annealing, directly following implantation, shows a non-linear dependence on the B-concentration in the films. At the end of annealing the W_2 :B and W:B films have the lowest amount of retained D. The pure W film does not follow the general trend of the other compositions which, after annealing, measure less retained D as the B-content decreases. The pure W-film breaks this trend as it has less D-loss after heat treatment as compared to both the W_2 :B- and W:B-films.

3.3. Post-annealing sample characterization

Aiming to better understand the different effects of the deuterium implantation in the films, ex-situ characterization was performed. SEM was used to study the surface morphologies of the films. It was possible to study the morphologies of the films for three cases, described in the following. Films grown simultaneously/under identical conditions as the implanted films were imaged to understand the film morphology directly after deposition (*As grown*). Since part of the films were intentionally covered by a steel washer during the implantations it was possible to investigate two separate regions of each sample (*Annealed only, Implanted & Annealed*). Fig. 5 shows SEM images of all films for the different stages/regions.

There were no significant morphological changes observed after annealing/implantation for the B film. The film was found to be amorphous by diffraction TEM, shown in Appendix A Fig. 6.

The Impl. & Annealed W:B9 sample shows what was suspected to be enrichment of W on the surface, which was later confirmed to be the case by HR-RBS seen in Fig. 6. The W-enrichment can be seen in the spectrum as a surface peak and measures 6.2×10^{15} at./cm². This W-enrichment is seen only in the implanted region and is thus likely a result of preferential sputtering of B during the D-irradiation, due to the difference in energy transfer in the binary collisions. This hypothesis is supported by sputter yields calculated by SRIM and are listed in Table 1 where the Wto-B sputter ratio is 1:66. Using this ratio and BS-corrected implantation fluences to calculate the difference in sputtered W and B, one would expect a W-enrichment of 2.06×10^{16} at./cm², which is almost twice of what was measured. SRIM is known to present unreliable sputtering yields at low ion energies due to a significantly higher energy threshold [41] but can still give a qualitative estimate of the preferential sputtering effect. Calculations done using the SDTrimSP software gave W-to-B sputter ratios of 1:600 (static simulation), which gives a W-enrichment of 2.2×10^{16} at./cm². One should note that the annealing of the sample could also have affected the distribution of the surface tungsten and could potentially contribute to the discrepancy observed between the simulated and experimental surface enrichment.

For the W:B film there are no noticeable differences between the *As grown* and *Annealed only* surfaces. The implanted region of the film however, shows cracks on the scale of 10–100 nm all over the surface. After cutting a lamella from the the *Impl. & Annealed* sample using FIB, it was confirmed by diffraction TEM to be mostly amorphous, with the

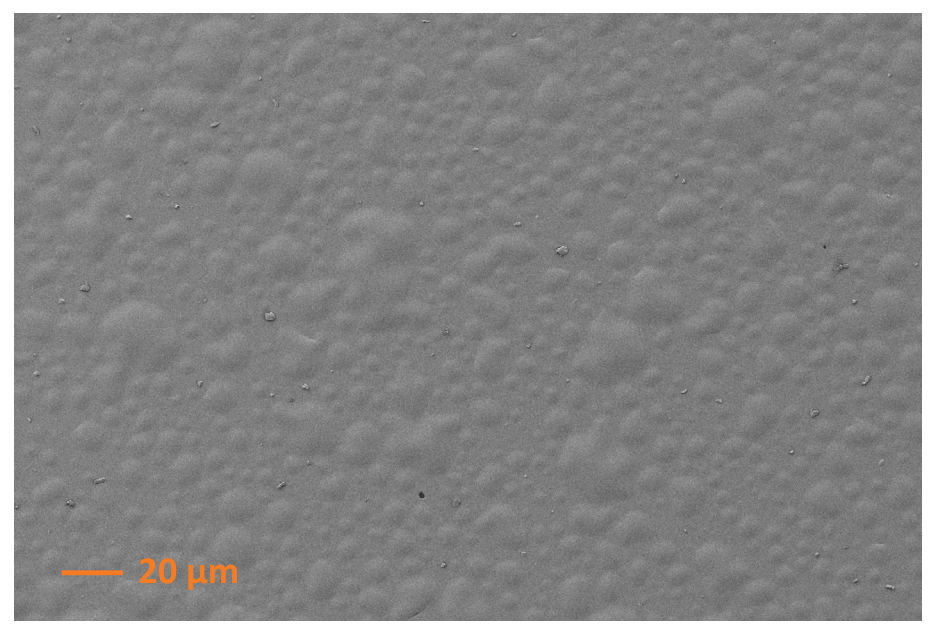


Fig. 7. SEM image showing bubble formation on surface of W-film after D-implantation and annealing of the sample.

presence of nanocrystals, shown in Appendix A Fig. 7. The cracks are clearly a result of the D implantation, but it is not obvious from the SEM images if this is due to implantation damage, or if the change in morphology is due to annealing and/or the presence of D in the W-B mixture.

For the W_2 :B film there were no significant differences visible between the $As\ grown$ and $Impl.\ \&\ Annealed$ stages. On the $Annealed\ only$ region of the same sample there are surface features visible that do not appear in the $As\ grown$ and $Impl.\ \&\ Annealed$ images. The cause of these features was not further investigated and it is possible that the imaged region is not representative of the surface morphology for the $Annealed\ only$ region of the sample. The film was found to be amorphous by diffraction TEM, after implantation and annealing, shown in Appendix A Fig. 8.

The W film was found to be polycrystalline in the SEM images, which was also confirmed by diffraction in TEM for the *As grown* sample, shown in Appendix A Fig. 9. The W film developed µm-sized bubbles in the *Impl. & Annealed* region of the sample, seen in Fig. 7. No bubbles were observed in the *Annealed only* region of the sample. Using FIB to see the cross section of one of the bubbles revealed that the film had delaminated completely from the substrate under the surface of the bubble, shown in Appendix A Fig. 10. The bubbles are believed to have formed due to the implanted D diffusing to the film-substrate interface forming pockets of D. Bubble formation in bulk W due to implantation of D has been investigated previously [44] but is different from what is seen in this case, where the bubbles were seen to form at the film-substrate interface, causing film delamination from the substrate.

4. Summary and conclusion

We present an investigation of the D-retention properties of sputter-deposited thin-films of W, B and mixtures of the two elements. It was observed, experimentally, how the impact of B influences the retention of implanted D in W, B and W-B mixtures. The retention behavior does not scale linearly with the atomic concentration of B in the mixtures, making it difficult to predict material properties based on simple scaling assumptions. The compositions also displayed considerably different surface morphologies, further highlighting the complexity of predicting how these materials will behave.

In this study, thin-films of W, B and W-B mixtures of three different stoichiometries were grown on Si-substrates using magnetron sputter-deposition. After pre-characterization by ToF-ERDA, the films were implanted with D followed by in-situ annealing up to 600 °C accompanied by simultaneous IBA measurements using RBS and ERDA to quantify the D content in the different samples. A region of each of the samples was covered during the implantation processes to shield the region from being implanted with D. This approach allowed for comparison between the surface morphologies of the implanted and non-implanted regions using SEM imaging techniques. SEM and TEM was also used to characterize twin samples that were neither implanted nor annealed for further comparison to the modified samples.

Deuterium retention directly after implantation was found to scale with B-content but does not depend linearly on the B-concentration in the mixtures. Aside results for the pure W sample and looking instead only at the amorphous films, there is evidence for a monotonic relation between B-concentration and D-retention for the compositions, both before and after annealing. The W-rich films retained significantly less D compared to the B-rich films, which showed much stronger D-retention properties. The films display different behaviors during annealing, where the B-rich films are more stable compared to the W-rich samples, retaining a large fraction of the implanted species to high temperatures. The W-rich films are desorbed to levels close to the detection limit before reaching 600 °C. The retention behavior of the pure-W film deviated from the trend observed for the other samples. SEM imaging revealed the formation of bubbles that are likely caused by diffusion of D to the film-substrate interface, which could also be an effect of the

polycrystalline structure of the pure-W film, confirmed by diffraction TEM and not seen for the other films. The incorporation of B seems to fully suppress the bubble formation observed in the pure-W film. The threshold B-concentration needed to suppress bubble formation is unclear from the presented results, further investigation of which could be of interest to explore as a follow-up study.

It was also observed that W-B mixtures can give rise to W-enrichment/crack formation on surfaces after annealing and implantation of high D fluences. These morphological changes were not observed in the non-implanted regions of the same samples, confirming that these changes are an effect of the D-implantation. The W-enrichment, confirmed by HR-RBS, was observed in the film with a W-to-B ratio of 1:9 and is expected to be the result of preferential sputtering of B during the D-irradiation. The crack formation occurred for a W-to-B ratio of 1:1 and is not thought to be an effect of preferential sputtering alone, due to the structure of the cracks which are reminiscent of thermal damage, but would need to be further studied to confirm.

CRediT authorship contribution statement

D.N. Gautam: Writing – review & editing, Writing – original draft, Visualization, Project administration, Methodology, Investigation, Formal analysis, Conceptualization. **T.T. Tran:** Writing – review & editing, Investigation. **M. Fellinger:** Writing – review & editing, Methodology, Investigation, Data curation. **F. Aumayr:** Writing – review & editing, Supervision. **M. Rubel:** Writing – review & editing, Conceptualization. **D. Primetzhofer:** Writing – review & editing, Supervision, Methodology, Conceptualization. **E. Pitthan:** Writing – review & editing, Visualization, Supervision, Project administration, Methodology, Investigation, Funding acquisition, Formal analysis, Conceptualization.

Declaration of competing interest

The authors declare that they have no known competing financial interests or personal relationships that could have appeared to influence the work reported in this paper.

Acknowledgements

This work has been carried out within the framework of the EURO-fusion Consortium, funded by the European Union via the Euratom Research and Training Programme (Grant Agreement No. 101052200—EUROfusion). Views and opinions expressed are, however, those of the author(s) only and do not necessarily reflect those of the European Union or the European Commission. Neither the European Union nor the European Commission can be held responsible for them. Accelerator operation was supported by the Swedish Research Council VR-RFI, Contract No. 2019_00191. This work was supported by the Swedish Energy Agency (Grant No. P202301345) and by KKKÖ (Commission for the Coordination of Fusion Research at the Austrian Academy of Sciences - ÖAW).

Appendix A. Supplementary data

Supplementary data to this article can be found online at https://doi. org/10.1016/j.nme.2025.102000.

Data availability

Data will be made available on request.

References

[1] R. Afanasenko, K. Vukolov, E. Andreenko, I. Orlovskiy, R. Rodionov, Radiation environment in ITER tokamak equatorial port 11, Fusion Eng. Des. 200 (2024) 114208, https://doi.org/10.1016/j.fusengdes.2024.114208.

- [2] J. Linke, et al., Challenges for plasma-facing components in nuclear fusion, Matter
- Radiat. Extrem. 4 (5) (Aug. 2019) 056201, https://doi.org/10.1063/1.5090100.
 N. Holtkamp, "An overview of the ITER project," *Proc. 24th Symp. Fusion Technol.*, vol. 82, no. 5, pp. 427–434, Oct. 2007, doi: 10.1016/j.fusengdes.2007.03.029.
- [4] S. Meschini, R. Delaporte-Mathurin, G.R. Tynan, S.E. Ferry, Impact of trapping on tritium self-sufficiency and tritium inventories in fusion power plant fuel cycles, Nucl. Fusion 65 (3) (Feb. 2025) 036010, https://doi.org/10.1088/1741-4326/ adacfa
- [5] P. Barabaschi, A. Fossen, A. Loarte, A. Becoulet, L. Coblentz, ITER progresses into new baseline, Fusion Eng. Des. 215 (Jun. 2025) 114990, https://doi.org/10.1016/ j.fusengdes.2025.114990.
- [6] A. Loarte et al., "Initial evaluations in support of the new ITER baseline and Research Plan," Tech. Rep. No ITR-24-004, 2024.
- [7] R. Dejarnac, et al., COMPASS-U plasma-facing components: Towards a full W first wall coverage, Fusion Eng. Des. 211 (Feb. 2025) 114815, https://doi.org/10.1016/ i-fusenedes 2025 114815
- [8] J. Bucalossi, et al., WEST full tungsten operation with an ITER grade divertor, Nucl. Fusion 64 (11) (Sep. 2024) 112022, https://doi.org/10.1088/1741-4326/ad64e5.
- [9] Y.-G. Kim, et al., Effect of impurities in vacuum vessels on the plasma parameters in inductive discharges, Vacuum 215 (Sep. 2023) 112330, https://doi.org/10.1016/j. vacuum 2023 112330
- [10] V.A. Shurygin, Light impurities: equilibrium, transport and density profiles in tokamak and stellarator plasmas, Plasma Phys. Control. Fusion 65 (10) (Aug. 2023) 105002, https://doi.org/10.1088/1361-6587/acef90.
- [11] E.J. Strait, et al., Progress in disruption prevention for ITER, Nucl. Fusion 59 (11) (Jun. 2019) 112012, https://doi.org/10.1088/1741-4326/ab15de.
- [12] R.A. Pitts, et al., Plasma-wall interaction impact of the ITER re-baseline, Nucl. Mater. Energy 42 (Mar. 2025) 101854, https://doi.org/10.1016/j. nme.2024.101854.
- [13] A. Loarte, et al., The new ITER baseline, research plan and open R&D issues, Plasma Phys. Control. Fusion 67 (6) (Jun. 2025) 065023, https://doi.org/10.1088/ 1361-6587/add9c9.
- [14] J. Winter, et al., Boronization in textor, J. Nucl. Mater. 162–164 (1989) 713–723, https://doi.org/10.1016/0022-3115(89)90352-8.
- [15] Y. Yamauchi, et al., Deuterium retention of low activation ferritic steel and boronized wall in JFT-2M, Fusion Eng. Des. 81 (1) (2006) 315–319, https://doi. org/10.1016/j.fusengdes.2005.09.031.
- [16] M.L. Apicella, et al., Effects of wall boron coating on FTU, an all metallic and carbon free medium size tokamak, Nucl. Fusion 45 (7) (Jun. 2005) 685, https:// doi.org/10.1088/0029-5515/45/7/018.
- [17] S.-H. Hong, et al., First boronization in KSTAR: Experiences on carborane, J. Nucl. Mater. vol. 415, no. 1(Supplement) (2011) S1050–S1053, https://doi.org/10.1016/j.inucmat.2010.10.059.
- [18] J.A. Snipes, et al., Initial design concepts for solid boron injection in ITER, Nucl. Mater. Energy 41 (Dec. 2024) 101809, https://doi.org/10.1016/j. nme.2024.101809.
- [19] X. Gao, et al., ICRF wall conditioning and plasma performance on EAST, Proc. 18th Int. Conf. Plasma-Surf. Interact. Control. Fusion Device, Jun. 390–391 (2009) 864–868, https://doi.org/10.1016/j.jnucmat.2009.01.226.
- [20] J. Li, et al., ICRF boronization a new technique towards high efficiency wall coating for superconducting tokamak reactors, Nucl. Fusion 39 (8) (Aug. 1999) 973. https://doi.org/10.1088/0029-5515/39/8/302.
- [21] A. Marin, et al., XPS post-mortem analysis of plasma-facing units extracted from WEST after the C3 (2018) and C4 (2019) campaigns, J. Nucl. Mater. 604 (Jan. 2025) 155525, https://doi.org/10.1016/j.jnucmat.2024.155525.
- [22] S. Abe, et al., Deuterium retention behaviors of boronization films at DIII-D divertor surface, Nucl. Mater. Energy 42 (Mar. 2025) 101855, https://doi.org/ 10.1016/j.nme.2024.101855.
- [23] S.A. Puyang, et al., Evolution of hydrogen isotopes retention behavior of in-situ boronization films in EAST, Nucl. Fusion 64 (7) (May 2024) 074001, https://doi. org/10.1088/1741-4326/ad4897.
- [24] D. Matveev, et al., Tritium removal from JET-ILW after T and D-T experimental campaigns, Nucl. Fusion 63 (11) (Oct. 2023) 112014, https://doi.org/10.1088/ 1741-4326/acf0d4.
- [25] T. Wauters, et al., Isotope removal experiment in JET-ILW in view of T-removal after the 2nd DT campaign at JET, Phys. Scr. 97 (4) (Mar. 2022) 044001, https:// doi.org/10.1088/1402-4896/ac5856.

- [26] Y. Yu, H. Sun, C. Wang, B. Cao, G. Zuo, J. Hu, Removal of deuterium retention by various helium discharge cleanings under strong magnetic field in EAST superconducting tokamak, Nucl. Mater. Energy 41 (Dec. 2024) 101834, https:// doi.org/10.1016/j.nme.2024.101834.
- [27] M. Abdullah, et al., Optimization of Wall-Conditioning Techniques on the MT-II Tokamak, Fusion Sci. Technol. 80 (6) (Aug. 2024) 731–740, https://doi.org/ 10.1080/15361055.2023.2241004.
- [28] Q. Tichit, et al., Plasma heat load in the toroidal gaps of the ITER-like plasma facing units in WEST tokamak, Nucl. Mater. Energy 42 (Mar. 2025) 101899, https://doi.org/10.1016/j.nme.2025.101899.
- [29] A. Grosjean, et al., First analysis of the misaligned leading edges of ITER-like plasma facing units using a very high resolution infrared camera in WEST, Nucl. Fusion 60 (10) (Sep. 2020) 106020, https://doi.org/10.1088/1741-4326/ab9fa6.
- [30] E. Pitthan, T.T. Tran, D. Moldarev, M. Rubel, D. Primetzhofer, Influence of thermal annealing and of the substrate on sputter-deposited thin films from EUROFER97 on tungsten, Nucl. Mater. Energy 35 (2023) 101449, https://doi.org/10.1016/j. nme.2023.101449.
- [31] P. Ström, D. Primetzhofer, Ion beam tools for nondestructive in-situ and inoperando composition analysis and modification of materials at the Tandem Laboratory in Uppsala, J. Instrum. 17 (04) (Apr. 2022) P04011, https://doi.org/ 10.1088/1748-0221/17/04/P04011.
- [32] K. Kantre, et al., SIGMA: a Set-up for In-situ Growth, Material modification and Analysis by ion beams, Nucl. Instrum. Methods Phys. Res. Sect. B Beam Interact. Mater. at. 463 (2020) 96–100, https://doi.org/10.1016/j.nimb.2019.11.007.
- [33] D. Rapp, P. Englander-Golden, D.D. Briglia, Cross Sections for Dissociative Ionization of Molecules by Electron Impact, J. Chem. Phys. 42 (12) (Jun. 1965) 4081–4085, https://doi.org/10.1063/1.1695897.
- [34] K. Kantre, et al., Combination of in-situ ion beam analysis and thermal desorption spectroscopy for studying deuterium implanted in tungsten, Phys. Scr. 96 (12) (Aug. 2021) 124004, https://doi.org/10.1088/1402-4896/ac1a88.
- [35] M. Seidl, H.L. Cui, J.D. Isenberg, H.J. Kwon, B.S. Lee, S.T. Melnychuk, Negative surface ionization of hydrogen atoms and molecules, J. Appl. Phys. 79 (6) (Mar. 1996) 2896–2901, https://doi.org/10.1063/1.361285.
- [36] V. Quillet, F. Abel, and M. Schott, "Absolute cross section measurements for H and D elastic recoil using 1 to 2.5 MeV 4He ions, and for the 12C(d,p)13C and 16O(d, p1)17O nuclear reactions," Nucl. Instrum. Methods Phys. Res. Sect. B Beam Interact. Mater. At., vol. 83, no. 1, pp. 47–61, 1993, doi: doi: 10.1016/0168-583X(93) 95906-I.
- [37] M. Mayer, SIMNRA, a simulation program for the analysis of NRA, RBS and ERDA, AIP Conf. Proc. 475 (1) (Jun. 1999) 541–544, https://doi.org/10.1063/1.59188.
- [38] S. A. Corréa, E. Pitthan, M. V. Moro, and D. Primetzhofer, "A multipurpose set-up using keV ions for nuclear reaction analysis, high-resolution backscattering spectrometry, low-energy PIXE and in-situ irradiation experiments," Nucl. Instrum. Methods Phys. Res. Sect. B Beam Interact. Mater. At., vol. 478, pp. 104–110, Sep. 2020, doi: 10.1016/j.nimb.2020.05.023.
- [39] J.F. Ziegler, M.D. Ziegler, J.P. Biersack, SRIM the stopping and range of ions in matter (2010), Nucl. Instrum. Methods Phys. Res. Sect. B Beam Interact. Mater. at. 268 (11) (2010) 1818–1823, https://doi.org/10.1016/j.nimb.2010.02.091.
- [40] Y.-R. Lin, S.J. Zinkle, C.J. Ortiz, J.-P. Crocombette, R. Webb, R.E. Stoller, Predicting displacement damage for ion irradiation: Origin of the overestimation of vacancy production in SRIM full-cascade calculations, Curr. Opin. Solid State Mater. Sci. 27 (6) (Dec. 2023) 101120, https://doi.org/10.1016/j. cossms.2023.101120.
- [41] H. Hofsäss, K. Zhang, and A. Mutzke, "Simulation of ion beam sputtering with SDTrimSP, TRIDYN and SRIM," Sel. Manuscr. Aris. 18th Int. Conf. Surf. Modif. Mater. Ion Beams SMMIB-2013, vol. 310, pp. 134–141, Aug. 2014, doi: 10.1016/j. apsusc.2014.03.152.
- [42] P. S. Szabo et al., "Graphical user interface for SDTrimSP to simulate sputtering, ion implantation and the dynamic effects of ion irradiation," Nucl. Instrum. Methods Phys. Res. Sect. B Beam Interact. Mater. At., vol. 522, pp. 47–53, Jul. 2022, doi: 10.1016/j.nimb.2022.04.008.
- [43] K. Sugiyama, K. Schmid, W. Jacob, Sputtering of iron, chromium and tungsten by energetic deuterium ion bombardment, Nucl. Mater. Energy 8 (Aug. 2016) 1–7, https://doi.org/10.1016/j.nme.2016.05.016.
- [44] Y. Xiang, B. Zhang, L. Shi, Evolution of bubble in tungsten irradiated by deuterium of low energy and high flux by molecular dynamics simulations, Appl. Surf. Sci. 606 (2022) 154715, https://doi.org/10.1016/j.apsusc.2022.154715.